Article

Compressible, anti-fatigue, extreme environment adaptable, and biocompatible supramolecular organohydrogel enabled by lignosulfonate triggered noncovalent network

Yihui Gu[1,2,3], Chao Xu[2,3], Yilin Wang[1], Jing Luo[1], Dongsheng Shi[1], Wenjuan Wu[1], Lu Chen[2], Yongcan Jin [1]✉, Bo Jiang [1]✉ & Chaoji Chen [2]✉

Achieving a synergy of biocompatibility and extreme environmental adaptability with excellent mechanical property remains challenging in the development of synthetic materials. Herein, a "bottom-up" solution-interface-induced self-assembly strategy is adopted to develop a compressible, anti-fatigue, extreme environment adaptable, biocompatible, and recyclable organohydrogel composed of chitosan-lignosulfonate-gelatin by constructing noncovalent bonded conjoined network. The ethylene glycol/water solvent induced lignosulfonate nanoparticles function as bridge in chitosan/gelation network, forming multiple interfacial interactions that can effectively dissipate energy. The organohydrogel exhibits high compressive strength (54 MPa) and toughness (3.54 MJ/m^3), 100 and 70 times higher than those of pure chitosan/gelatin hydrogel, meanwhile, excellent self-recovery and fatigue resistance properties. Even when subjected to severe compression up to a strain of 0.5 for 500,000 cycles, the organohydrogel still remains intact. This organohydrogel also demonstrates notable biocompatibility both in vivo and vitro, environment adaptability at low temperature, as well as recyclability. Such all natural organohydrogel provides a promising route towards the development of high-performance load-bearing materials.

Soft load-bearing tissues (muscles, ligaments, cartilage) possess precisely tuned mechanical properties that enable them to withstand body stress and endure repeated cycles of stretching and movement[1,2]. To mimic the soft, tough, and impact-resistant properties of soft load-bearing tissues, hydrogels based on noncovalent bonding (hydrogen bonding[3], ionic bond[4], ligand bonding[5], etc.) have been widely explored. By integrating a range of these noncovalent interactions into the hydrogel network, the resulting hydrogels exhibit enhanced mechanical properties including high tensile and compressive strength, as well as high Young's modulus. However, a common limitation among many of these hydrogels is the absence of a mechanism for rapid recovery after deformation. Conventional physically

[1]Jiangsu Co-Innovation Center of Efficient Processing and Utilization of Forest Resources, College of Light Industry and Food Engineering, Nanjing Forestry University, Nanjing 210037, China. [2]Hubei Biomass-Resource Chemistry and Environmental Biotechnology Key Laboratory, Hubei Provincial Engineering Research Center of Emerging Functional Coating Materials, School of Resource and Environmental Sciences, Wuhan University, Wuhan 430079, China. [3]These authors contributed equally: Yihui Gu, Chao Xu. ✉e-mail: jinyongcan@njfu.edu.cn; bjiang@njfu.edu.cn; chenchaojili@whu.edu.cn

crosslinked multi-networks and hybrid networks typically exhibit a lengthy recovery cycle when stressed. While some long polymer chain hydrogels can recover quickly, they often suffer from reduced strength due to their intrinsic interactions[6]. Consequently, synthesizing load-bearing materials that meet all the requirements for biomedical applications remains a formidable challenge. Biocompatibility, biodegradability, and extreme-environment-adaptability are essential requirements for load-bearing materials, while the materials must also be strong enough to resist physical stresses and support normal human activities.

From a sustainability perspective, abundant and non-toxic biomass materials such as chitosan[7], gelatin proteins[8], cellulose[9], and sodium alginate[10] have flourished in the biomedical field, while it is often difficult to achieve high mechanical properties with a single material. Therefore, researchers often make up for their shortcomings by compositing a variety of natural materials with mechanical properties far exceeding those obtained from simple mixtures of their respective constituent materials[11]. This approach relies on tightly coupled separated phases with significant differences in modulus, which ensure limited inelastic deformation, bridging, and effective energy dissipation to achieve the working mechanism of "hard-phase reinforcement and hard-soft-phase synergistic toughening". The combination of stiffness, toughness, strength, and fatigue resistance in hydrogels allows for diverse applications, such as soft robots[12], implantable devices[13], and artificial muscle cartilage[14]. Nevertheless, synthesizing hydrogel materials with multiple mechanical properties remains challenging as high stiffness, toughness, and fast recovery often present conflicting requirements.

In recent years, numerous methods have emerged for improving the structure of hydrogels to increase their strength and toughness, including the construction of homogeneous networks[15,16], the introduction of sacrificial bonds[17–19], nanomaterials composites[20,21], and induced microphase separation[22,23]. Among these approaches, two of the most effective methods involve improving network homogeneity and employing sacrificial bonds. Constructing a homogeneous gel network serves to mitigate stress concentration and improve compressive strength and toughness to some extent. However, this approach has limited effectiveness for materials that already contain cracks or imperfections. Sacrificial bonding, on the other hand, utilizes the non-uniformity of the gel network to generate energy dissipation. Typical examples are the construction of bi-network gels with heterogeneous structures and complementary properties, where highly crosslinked rigid frameworks can efficiently dissipate energy by breaking bonds, while sparsely crosslinked ductile frameworks can withstand a wide range of strains, but the increase in rigidity is often at the cost of a decrease in toughness[24,25]. The reinforcing and toughening effect of hydrogels is usually limited for specific methods of structural improvement.

Unlike conventional bi-networks, we designed a connected network organohydrogel with enhanced interactions and synergistic dissipative mechanisms to tune the time-domain expression of noncovalent interactions between bi-networked polymers. This approach was achieved by incorporating nanoparticles and inducing microphase separation through a straightforward solvent exchange strategy. Specifically, we employed a feasible "soaking" method in lignosulfonate-ethylene glycol (SL-EG) solution to transform weak chitosan-gelatin (C-G) composite hydrogels into robust chitosan-lignosulfonate-gelatin (C-SL-G) linked-network organohydrogels (Fig. 1a). Chitosan serves as the hard phase to enhance the mechanical strength of the organohydrogels, inhibit the rate of crack expansion during fracture, and maintain the integrity of the material. Gelatin, on the other hand, functions as the ductile soft phase to take up most of the load in the event of molecular strand breakage of the chitosan chains. The differences in the distribution states of the polymers in water and EG were utilized to modulate the interfacial interaction forces across the network, inducing the formation of a uniform and robust polymer network[26]. The resulting C-SL-G organohydrogel can be compressed up to 0.9 without rupture, and maintain the original shape even after undergoing repeated 500,000 cycles at strain of 0.5 (Fig. 1b, c). Notably, the resultant tough organohydrogels display noticeable resistance to icing and offer moisturizing properties, attributed to the non-volatile nature of EG. Moreover, the C-SL-G organohydrogel with all natural components facilitates scalability through a straightforward and green "soaking" method, enabling the material and process with good sustainability, recyclability, and cost effectiveness for commercialization and large-scale application (Fig. 1c, d and Supplementary Tables 1-5). The commendable biocompatibility and biodegradability of chitosan, gelatin, and lignin, coupled with the excellent mechanical strength, fatigue resistance, and extreme environmental adaptability, open up an avenue for the advancement of robust interconnected biomedical hydrogels. Furthermore, this strategy has the potential for extension to other solvents such as lignin-glycerol solution and metal ion-EG/glycerol solution to prepare resilient multifunctional organohydrogels suitable for various applications.

Results

Construction, structure, and morphology of C-SL-G organohydrogels based on conjoined network

To obtain organohydrogels crosslinked with SL and EG, we employed a gel soaking strategy. Initially, a combination of gelatin and chitosan was heated and stirred until dissolved to obtain a mixed solution, which was then cooled by low temperature to obtain a soft and brittle C-G composite hydrogel. Subsequently, hydrogels were immersed in SL-EG solution to obtain C-SL-G organohydrogels (Supplementary Fig. 1). During the soaking process, the SL particles infiltrate to act as intermediary crosslinking points involved in the noncovalent crosslinking of the polymer network[27,28]. The process is accompanied by a noticeable color change from light yellow to dark brown, reflecting the introduction of SL into the gel interior during solvent exchange (Supplementary Fig. 2). Thus, the salt concentration of C-SL-G organohydrogels can be easily adjusted by modifying the fabrication conditions, such as sample size and immersion time. These results demonstrate the excellent performance of dual network linked organohydrogels. The inexpensive substrate and simple preparation process make it more competitive for commercialization and large-scale application (Supplementary Fig. 1). The developed organohydrogel also demonstrates excellent recyclability (Supplementary Fig. 3). Through a simple procedure involving solvent exchange with water under heating and stirring conditions, a uniformly mixed solution of the organohydrogel components can be obtained. In addition, owing to the fracture/reconstruction characteristics of noncovalent bonds, the hydrogel can be further reconstituted through water evaporation and gelatinization. Finally, immersion of this regenerated hydrogel into EG for sufficient solvent exchange leads to the regeneration of organohydrogel.

Scanning electron microscopy (SEM) was performed to observe the morphological structure of the gels. The pristine C-G hydrogels showed a continuous honeycomb-like porous structure with thin walls (Fig. 2a). The increased swelling degree after solvent exchanges with EG (Supplementary Fig. 4) reveals EG molecules can penetrate the interior network structure, leading to volume expansion and stretching of the polymer network. However, the EG penetration also resulted in a rough morphology (Fig. 2b and Supplementary Fig. 5a)[29]. Upon the introduction of lignin, the structure of C-SL-G organohydrogels became denser and more stable, as demonstrated in Fig. 2c, d and Supplementary Fig. 5b, c. The addition of lignin makes it act as a bridging molecule to provide abundant crosslinking points with polymer chains through strong noncovalent bonds, thus leading to a dense structure for C-SL-G organohydrogels.
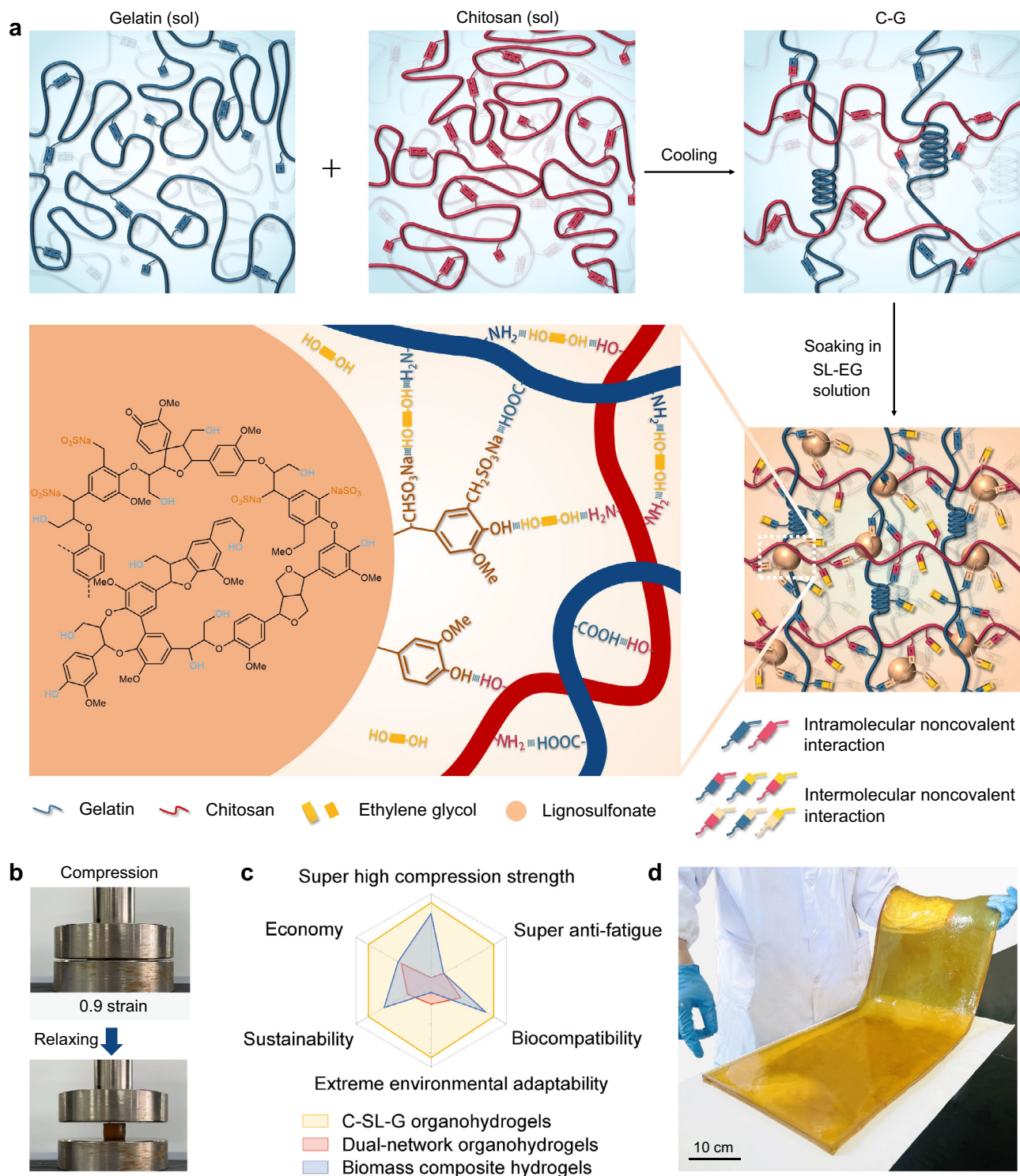
Fig. 1 | Construction strategy and key features of the C-SL-G organohydrogels.
a Schematic representation of the preparation of C-SL-G organohydrogels.
b Optical images of the C-SL-G organohydrogel in compressed and released states.
c Radar chart of the combined benefits of C-SL-G organohydrogels, dual-network organohydrogels, and biomass composite hydrogels (where '1' represents the type of SL, and '0.01' signifies the initial concentration of the immersion solvent in g/mL). **d** Optical image of the C-SL-G organohydrogel.

The distribution of EG and SL within the polymer network was investigated using two-dimensional Raman analysis (Fig. 2e–h and Supplementary Fig. 6). The C-H bending vibration at 1457 cm^{-1}, as well as the CH$_2$ stretching vibration and O-H stretching vibration at 2900–3500 cm^{-1}, provided insights into the distribution of the EG structure. Comparative analysis reveals a higher EG content in the C-G-EG organohydrogel compared to the C-SL-G organohydrogel, possibly attributed to the inhibitory influence of SL[30]. The crosslinking density of C-SL-G organohydrogels was higher compared to C-G-EG organohydrogels without SL (Supplementary Fig. 7). This observation clearly demonstrates that SL acts as a reinforcing agent in the subtle interaction with the polymer network, which is further confirmed by X-ray diffraction (XRD). Supplementary Fig. 8 depicts the XRD spectra of chitosan, gelatin, C-G-EG and C-SL-G organohydrogels, showcasing
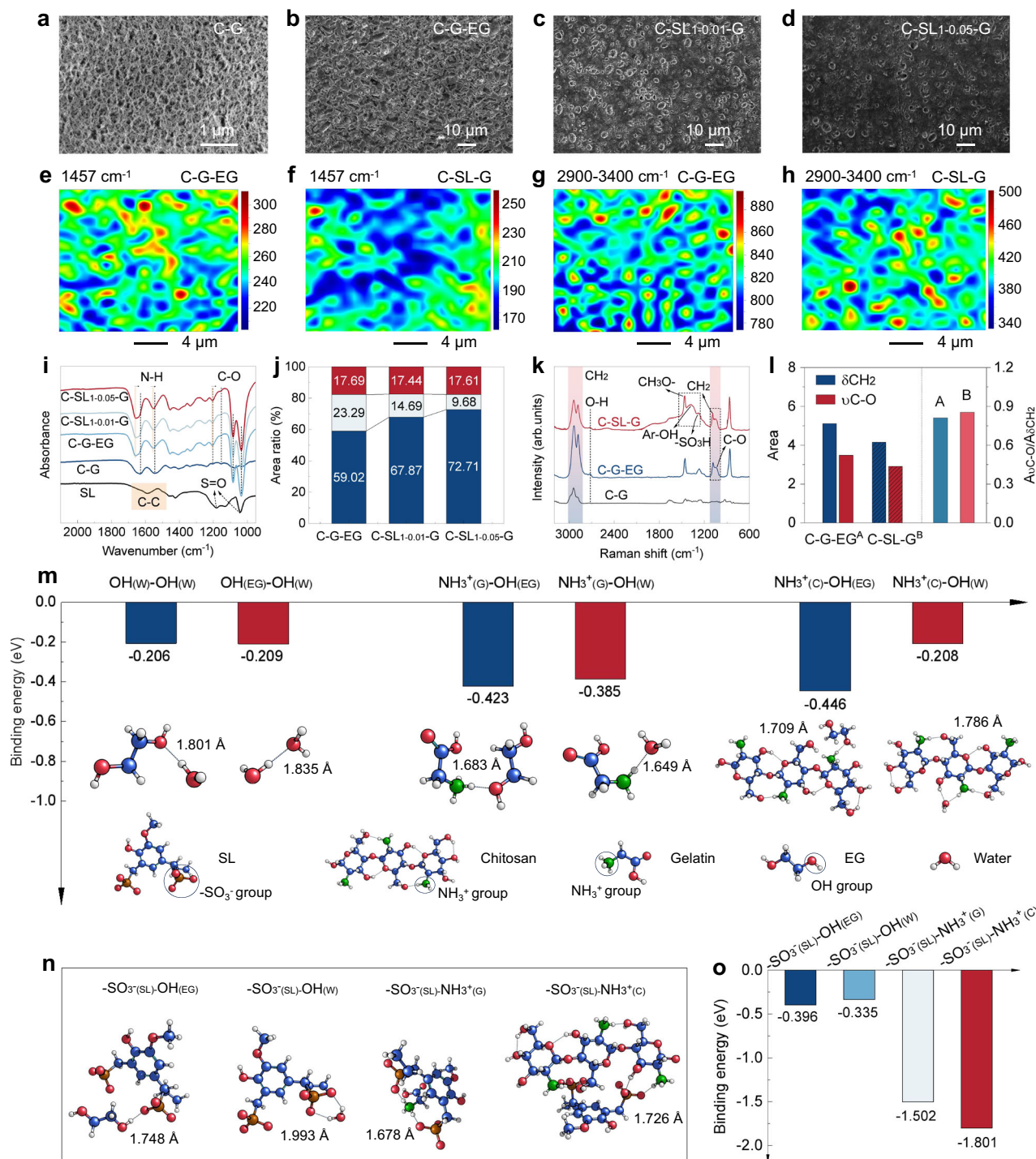
Fig. 2 | Structure and morphology features of the conjoined-network organo-hydrogels. Representative SEM images of original C-G hydrogel (**a**), C-G-EG (**b**) and C-SL-G organohydrogels with 0.01 g/mL (**c**), 0.05 g/mL (**d**) SL-EG immersion by supercritical drying. Two-dimensional (2D) Raman images of C-SL-G organohydrogels without SL (**e**) and with SL (**f**) obtained from the bending vibrations of C-H bonds (1457 cm⁻¹). Two-dimensional (2D) Raman images of C-SL-G organohydrogels without SL (**g**) and with SL (**h**) obtained from the CH₂ stretching vibration and O-H stretching vibration (2900-3400 cm⁻¹). **i** FTIR spectra of SL, C-G hydrogel, C-G-EG, and C-SL-G organohydrogels. **j** Ratio of bulk H₂O molecules, clustered EG-H₂O, and isolated EG in three groups of organohydrogels. **k** Raman analysis of C-G, C-G-EG, and C-SL-G organohydrogels. **l** Area and proportion of C-O band symmetric stretching vibration and CH₂ band rocking (1000-1100 cm⁻¹). **m** Calculation of binding energy and energy-optimized geometries of noncovalent bonding between OH (EG), OH (water), NH₃⁺ (chitosan), NH₃⁺ (gelatin) by DFT. **n** Energy-optimized geometries of noncovalent bonding between SO₃⁻ (SL) and OH (EG), OH (water), NH₃⁺ (chitosan), NH₃⁺ (gelatin), respectively, obtained by theoretical calculations from DFT studies. **o** Calculation of binding energy between SO₃⁻ (SL) and OH (EG), OH (water), NH₃⁺ (chitosan), NH₃⁺ (gelatin), respectively by DFT.

sharper characteristic peaks at 20°, indicative of a more organized structure facilitated by SL embedding[31,32].

Fourier transform infrared (FTIR), X-ray photoelectron spectroscopy (XPS) and Raman spectroscopy were performed to get a comprehensive understanding of the interactions between lignin, bisolvent, chitosan, and gelatin (Fig. 2i–l, Supplementary Figs. 9, 10 and Supplementary Tables 6–8). The red shift of the C-O peak at 1035–1200 cm⁻¹ after the introduction of EG, alongside the slight shift of

the characteristic peaks of N-H at 1629 and 1545 cm^{-1} towards lower wavelengths after the introduction of lignin, confirm the generation of hydrogen bonding. To verify the role of EG, we fitted the C-G-EG, C-SL$_{1-0.01}$-G, and C-SL$_{1-0.05}$-G located in the range of the characteristic peaks of 2500–4000 cm^{-1}. In the C-G-EG organohydrogel, a peak located at 3428 cm^{-1} confirms the presence of strong hydrogen bonding between EG and H_2O molecules[33,34]. With the incorporation of SL, the wavenumber of the O-H stretching vibration gradually increases, while the intensity gradually decreases and broadens. The higher wavenumber suggests elevated energy of O-H bonds, attributed to the destruction of hydrogen bonds between EG and water by hydrophilic SL. The ratio of the two H_2O conformations, calculated from the fitted peak areas, reveals insights into the FTIR spectra. Following the introduction of SL, the associated O-H content increases to 67.87% and 72.71%, respectively. This indicates that the addition of lignin leads to the enhancement of bulk H_2O-H_2O hydrogen bonding operation in the system. Furthermore, the binding energy strength of the -OH and -NH_2 of chitosan, as observed in XPS, decreases with the introduction of lignin, which provides compelling evidence of strong noncovalent bonding interactions between -NH_2 and -OH and -SO_3H in chitosan and gelatin[35,36].

To further verify the crucial roles of EG and lignin within this system, laser Raman was employed to investigate the EG-H_2O system in organohydrogels (Fig. 2k). Firstly, in the gel system containing lignin, the obviously attenuated EG characteristic peaks are similar to the FTIR results. The area ratio of C-O symmetric stretching vibration to CH_2 rocking vibration peaks as shown in Fig. 2l reveals significant changes after the introduction of SL[37]. The introduction of SL hinders the formation of intermolecular EG-H_2O hydrogen bonding and forms a large number of hydrogen bonds with solvent molecules and the polymer network. Consequently, the C-O symmetric stretching vibration of EG molecules exhibits a notable increase, attributed to the release of the hydroxyl groups in molecules and the weakening of the hydroxyl groups in the water molecules. As shown in Supplementary Fig. 11, the introduction of EG and SL into the aqueous chitosan-gelatin solution increases the energy storage modulus (G′) and complex viscosity (η*) in the platform region. The G′ and η* values for the C-SL-G organohydrogel samples peak in the platform region, indicating that the densest physically crosslinked network based on noncovalent bonding is formed in the presence of SL[38–40].

The density functional theory (DFT) simulations show that the hydroxyl groups in EG exhibit stronger binding energies with chitosan and gelatin than the interactions between water molecules and polymer networks (Fig. 2m). This strong interaction fosters hydrogen bonding between EG and polymers. In the structural model, the bond energies between EG and gelatin/chitosan molecules are −0.423 eV and −0.446 eV, respectively, greater than those observed between water molecules and gelatin/chitosan, indicating that they are more likely to bond and form a more compatible molecular structure with the polymer chain[41]. In Fig. 2n and o, the binding energies of SO_3^- and NH_3^+ (chitosan and gelatin) in lignin are −1.801 eV and −1.502 eV, respectively, much higher than those between other structures. The corresponding bond lengths are 1.726 Å and 1.678 Å, respectively, lower than EG/water molecules. These findings suggest that the SL is able to crosslink quickly and efficiently with the polymer network in solvent substitution to form stronger interactions, enhancing the overall structure of the polymer network. Therefore, lignin molecules serve as crosslinking points or physical fillers in the polymer network. These new crosslinking points or fillers provide additional mechanical support, thereby increasing the deformation resistance of the hydrogel and improving its morphological stability.

Mechanical properties of the C-SL-G conjoined-network organohydrogels

The interconnected network formed among chitosan, gelatin, SL, and EG might contribute to the excellent mechanical properties of C-SL-G organohydrogels, rendering them well-suited for use as load-bearing materials. The compression strength of the C-SL-G conjoined-network organohydrogel can be readily tuned by adjusting the concentration of the immersion solution. As shown in Fig. 3a, the compressive strength of the hydrogel reaches a maximum of 54 MPa after being immersed in SL$_{1-0.01}$-EG solution, which is about 100 times higher than that of the original C-G hydrogel (0.52 MPa). Furthermore, a substantial enhancement in compressive toughness is attained, representing an approximate increase of 70 times (Fig. 3b). Notably, the mechanical properties of C-SL-G organohydrogel surpass those of other biopolymer gels and organohydrogels, and even exceed those of natural cartilage. Due to its unique dual network structure, a combination of high rigidity and high toughness is achieved (Fig. 3c and Supplementary Tables 9, 10).

The elastic modulus of C-SL-G organohydrogels increases with the rise in lignin content. The gel stiffness is positively correlated with the lignin content within a certain range, influenced by the benzene ring structure of lignin rigidity. EG enhances the hydrogen bonding between polymer networks. When glycerol, which contains three hydroxyl groups, is chosen for solvent exchange, the resulting hydrogels exhibit higher compressive strength, modulus, and toughness compared to the C-G-EG organohydrogel (Supplementary Fig. 12). This highlights the crucial role of hydrogen bonding within the system. With the introduction of lignin in the gel network, strong interfacial interactions are developed. Lignin acts as shared interconnection points that reinforce the gel network and interweave with each other, effectively dispersing the stress throughout system. Conversely, hydrogels with a higher proportion of SL exhibit decreased compressive strength and toughness due to lignin's self-aggregation, causing uneven stress dispersion throughout the network and limiting the mechanical properties of the organohydrogels[23,37]. This also explains the trend of increasing and then decreasing tensile properties of organohydrogels (Supplementary Fig. 13). The rheological behavior of the organohydrogels further supports these findings. The G′ and loss modulus (G″) gradually increase with the introduction of EG and SL, exhibiting their higher stiffness or rigidity. Moreover, the gradual increase in the composite viscosity suggests the gradual enhancement of intermolecular interactions in the organohydrogels. These results underscore the effective enhancement of mechanical properties and stability achieved through the incorporation of EG and SL (Supplementary Figs. 14 and 15).

Figure 3d illustrates the good deformability and resilience of the C-SL-G organohydrogel, which can be easily twisted, knotted, folded and easily withstands a weight of 500 g with minimal deformation (Supplementary Fig. 16). Figure 3e shows pictures of the puncture deformation test, clearly demonstrating that the C-SL-G organohydrogel can endure high levels of localized stress without visible damage or permanent deformation, underscoring its excellent mechanical properties combining both high strength and toughness. Moreover, when four gels of the same size (1.5 cm in length, width, and height) are used as a stand, the upper portion supporting a flat plate can bear the weight of a 70 kg human body, which is equivalent to 3500 times the weight of a single gel itself (Fig. 3f).

Furthermore, the macro- and microstructural analysis of the material during compression were conducted using small-angle X-ray scattering (SAXS) and wide-angle X-ray scattering (WAXS) (Supplementary Figs. 17 and 18). The size Gaussian distribution curves are calculated by SAXS one-dimensional intensity distribution. Our findings reveal that the introduction of SL results in smaller and more spatially dense pores, unaffected by the compression process, suggesting that numerous hydrogen bonds are continuously broken and reorganized. WAXS analysis indicates the presence of a highly crystalline structure. With the compression strain increasing, the scattering patterns still show a strong amorphous scattering ring, confirming that the compression process does not induce the formation of an
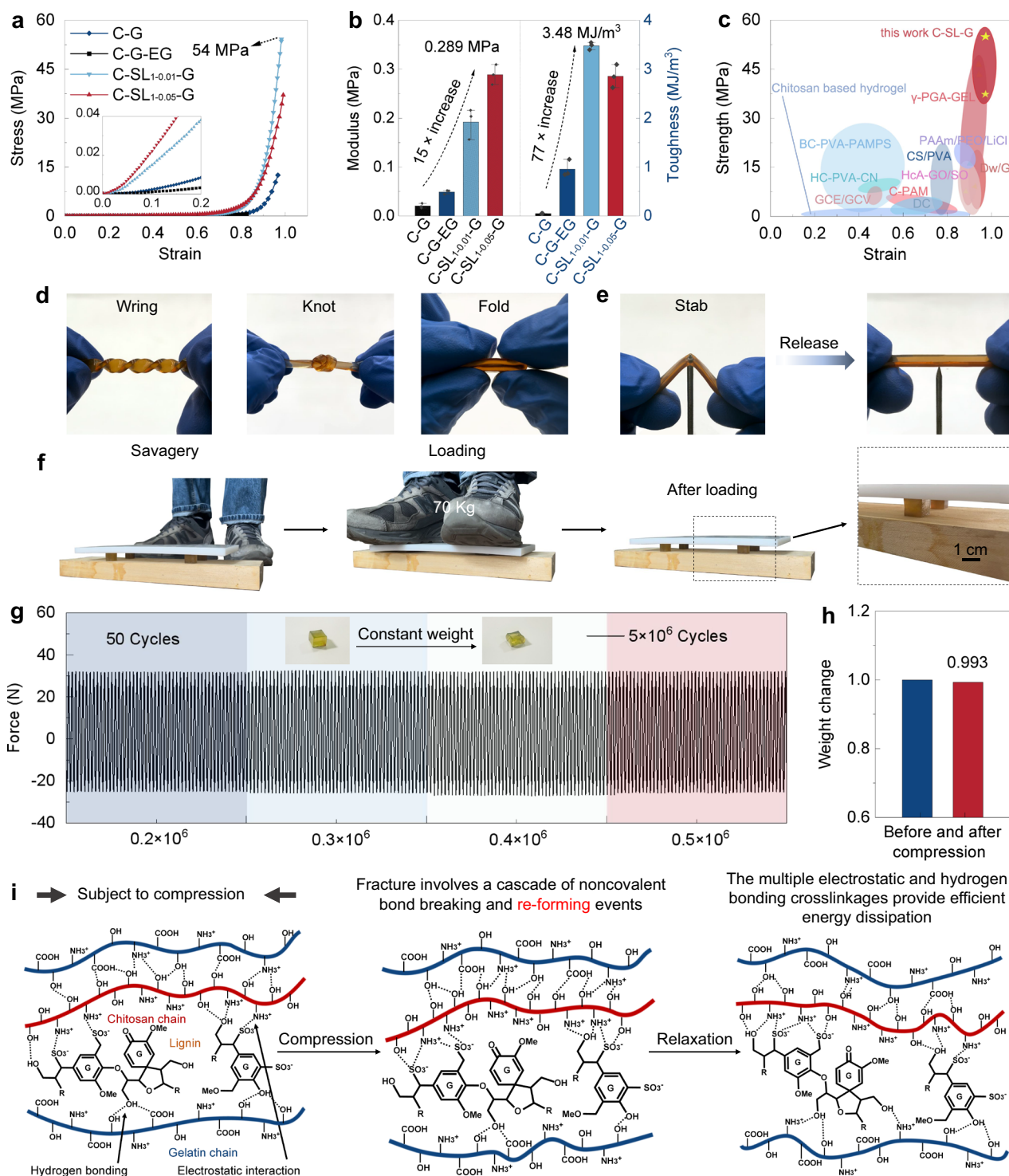
Fig. 3 | Mechanical properties of the C-SL-G organohydrogels. a Compressive stress-strain curves (inset shows magnified plot in the low-strain region) and **b** modulus and compressive toughness of the C-G hydrogel after soaking in SL₁-EG solutions at various concentrations. Values in **b** represent their means ± SDs from $n = 3$ independent samples. **c** Comparison plots of C-SL-G organohydrogels in this work with other tough hydrogels by strength versus strain. **d** Photographs of the C-SL-G organohydrogel subjected to various external forces. **e** Photographs of the C-SL-G organohydrogel pierced with nails. **f** Photograph of the C-SL-G

organohydrogel supporting the weight of a human body in which the structure maintains intact after loading. **g** Force-frequency curve of the C-SL-G organohydrogel over 500,000 consecutive spaceless loading-unloading cycles at constant strain (ε = 0.5). **h** Weight change of the C-SL-G organohydrogel with 500,000 successive loading-unloading cycles without interval under a constant strain (ε = 0.5). **i** Mechanism diagram of self-recovery and anti-fatigue ability: during compression-recovery, noncovalent bond breaks, and new bonds were formed.

oriented structure. In addition, a unique peak at $q = 15.3$ nm^{-1} indicates a lattice spacing of 4.1 Å in the pristine state and 4.124 Å in the compressed state, suggesting that unidirectional compressive stress leads to a longer lattice spacing.

Interestingly, by introducing Cu^{2+} in addition to lignin, the robust metal coordination bond is leveraged, known for its good toughening properties. This dual reinforcement approach results in even more notable mechanical properties for organohydrogels, with compressive

strength reaching up to 60 MPa and tensile strength up to 0.7 MPa, as shown in Supplementary Fig. 19. This highlights the significant impact of noncovalent bonds in improving the mechanical properties of the gels[42].

Achieving ultrahigh self-resilience and fatigue resistance is paramount for gels to maintain daily cyclic loading and longevity. As a load-bearing material, C-SL-G organohydrogel requires sufficient modulus to maintain structural stability[18,43]. At compression strains of 0.5 and 0.6, the C-SL-G organohydrogel maintains excellent stability with negligible mass change even after 500,000 and 200,000 high-frequency compression cycles, respectively (Fig. 3g, h and Supplementary Fig. 20). This is also verified in 100,000 high-frequency tensile cycles (Supplementary Fig. 21). Notably, even at strain as high as 0.8, the C-SL-G organohydrogel maintains a stable structure after 3000 high-frequency compression cycles, demonstrating its excellent fatigue resistance. The compressed C-SL-G organohydrogel can also rapidly recover, proving its self-recovery properties (Supplementary Fig. 22). The mechanical properties of C-SL-G organohydrogels were thoroughly investigated by uninterrupted cyclic loading-unloading tests under multiple conditions. Even when subjected to a high compression ratio of above 0.9, the samples consistently maintain high load-bearing capacity and stable weight (Supplementary Fig. 23). Meanwhile, they exhibit high mechanical properties in the unilateral notch test and can resist crack extension, which verifies their excellent damage and fatigue resistance under high pressure loading (Supplementary Fig. 24).

At compressive strain of 0.2, 0.4, and 0.6, the C-SL$_{1-0.01}$-G organohydrogel shows minimal hysteresis loops and excellent elasticity (Supplementary Fig. 25a, b). Supplementary Fig. 25c and d summarize the recovery behavior of C-SL$_{1-0.01}$-G organohydrogel after different relaxation times. The recovery ability of the organohydrogel maintains at a high level (>88%) for five consecutive time periods, indicating that the broken hydrogen bonds and electrostatic forces can be basically restored to the original state within a certain timeframe. Moreover, in successive cycles at a constant strain, numerous hysteresis lines were observed in consecutive cycles, with subsequent cycles exhibiting lower energy dissipation but consistent presence of hysteresis lines. This suggests that successive reorganizations of noncovalent bonds can partially restore the material (Supplementary Figs. 25e, f and 26-28). These results imply that the disrupted amino-SL electrostatic cross-linked structural domains and the amino-EG hydrogen-bonded cross-linked structural domains can be reasonably restored to their original or otherwise accessible positions within a relatively short time after compression (Fig. 3i and Supplementary Fig. 29)[44].

Strengthening mechanisms of the C-SL-G organohydrogels

Theoretical studies have suggested that SL acts as a reinforcing phase (mechanical strength) in polymer composites. To gain a deeper understanding of how the components synergistically contribute to the mechanical properties of C-SL-G organohydrogels, we investigated the morphological changes of lignin introduced into the gel using particle size analysis and transmission electron microscopy (TEM) (Fig. 4a, b). The results reveal that during the self-assembly process, lignin molecules undergo a transformation into spherical particles. This transformation is attributed to long-range interaction forces, particularly π-π stacking and hydrogen bonding. The polarity difference between the components contributes to the formation of these spherical particles, leading to a reduction in the average particle size from 240 nm to 150 nm[45,46]. In addition, the interfacial cohesion and structural stability of C-SL-G composites were investigated by molecular dynamics simulations (Supplementary Data 1). The number of hydrogen bonds and the intermolecular correlations are analyzed in 20 ns. These simulations reveal that the intermolecular interactions between the two different components of the gel are C-SL-G > C-G > C-G-EG, as shown in Supplementary Fig. 30. Likewise, the number of

hydrogen bonds is C-SL-G > C-G-EG > C-G, as shown in Fig. 4c. The specific energies and the number of hydrogen bonds are presented in Supplementary Table 11. The intra-polymer and inter-polymer interactions in this exogel constructed by solvent exchange strategy are initially suppressed due to the presence of EG but recovered in the presence of lignin, leading to optimization and re-crosslinking of the polymer network. The success of this approach relies on a suitable solvent, which helps to stretch the polymer conformation and homogenize the network[26,47].

Zeta potential measurement was carried out to evaluate the change of electric potential after lignin introduction (Fig. 4d), which provides evidence of electrostatic interaction between lignin and chitosan. The charge of the chitosan solution gradually decreases with SL addition. This indicates that there is a strong electrostatic interaction between SL and chitosan. To demonstrate the important role of sulfonic acid groups in the enhancement of toughening, two kinds of lignin nanoparticles with different sulfonation (2.9, 0.9 mmol/g) were prepared. The success of the modification was confirmed through infrared analysis (Supplementary Fig. 31), and the structure of the two kinds of lignin, as well as the content of phenolic hydroxyl and sulfonate groups, were analyzed and quantified by two-dimensional nuclear magnetic resonance (2D-NMR), ^{31}P NMR spectrometry, and potentiometric titration, respectively (Fig. 4e and Supplementary Figs. 32, 33). The sulfonation does not change the phenolic hydroxyl content because the reaction sites occurred in the C_5 and C_α positions of the lignin phenylpropane structure, and the SL$_1$ with a high degree of sulfonation (2.9 mmol/g) was found to be more advantageous in compressive and tensile test (Fig. 4f and Supplementary Fig. 34). This discovery offers compelling evidence that sulfonate groups play a pivotal role in strengthening lignin, thereby enhancing toughness.

Low-field NMR spectroscopy was used to investigate the presence state of water within the gel and the interaction between water and polymer (Fig. 4g–i). The relatively rapid free induction decay (FID) of the C-SL-G organohydrogel can be attributed to the SL in the network that acts as crosslinking points, generating a large number of noncovalent crosslinks (the rigid component), which results in a rapidly decaying FID signal. A linear combination of the Weibull function and two exponential functions was applied to fit the FID data, allowing for the determination of apparent spin relaxation time (T_2) values and their relative fractions[48–50]. $T_{2, rigid}$, $T_{2, inter}$, and $T_{2, mobile}$ represent the relaxation times of the rigid, intermediate, and mobile components, respectively, and the f_{rigid}, f_{inter}, and f_{mobile} represent the corresponding proton fractions, respectively. The f_{rigid} values of all three gels were lower than 5%, indicating a strong interaction between the polymer and the solvent. f_{mobile} is the main form of water in the C-G hydrogel, representing the free water that is not tightly bonded to the polymer. After solvent exchange, the appearance of the three fractions may be caused by the relatively weak binding between EG and water (compared with the interaction between polymer and water). The migration of water with higher degree of freedom to water with lower degree of freedom indicates that the water in the sample becomes more tightly bound to the polymer. The $T_{2, rigid}$ decreases with the introduction of EG and SL, and the $T_{2, inter}$ of the C-SL-G organohydrogel is only 1/2 of that of the C-G-EG organohydrogel. This suggests that the EG restricts the solvent molecules within the hydrogel and forms a weak bond with the polymer, while the SL introduction further causes restricted solvent movement and strengthens the interaction between the gel network and the solvent molecules[51,52].

To quantitatively assess the intermolecular interactions between chitosan and SL, atomic force microscopy (AFM) was conducted (Fig. 4j–l), where smooth spin-coated SL-H$_2$O/EG (SL$_1$-H$_2$O, SL$_1$-H$_2$O/EG, and SL$_2$-H$_2$O/EG) surfaces were tapped with a chitosan coated silicon probe, respectively. The adhesion force between the tip and the contacting surfaces was recorded during the separation process, with each measurement repeated for 500 times to obtain the contours of the
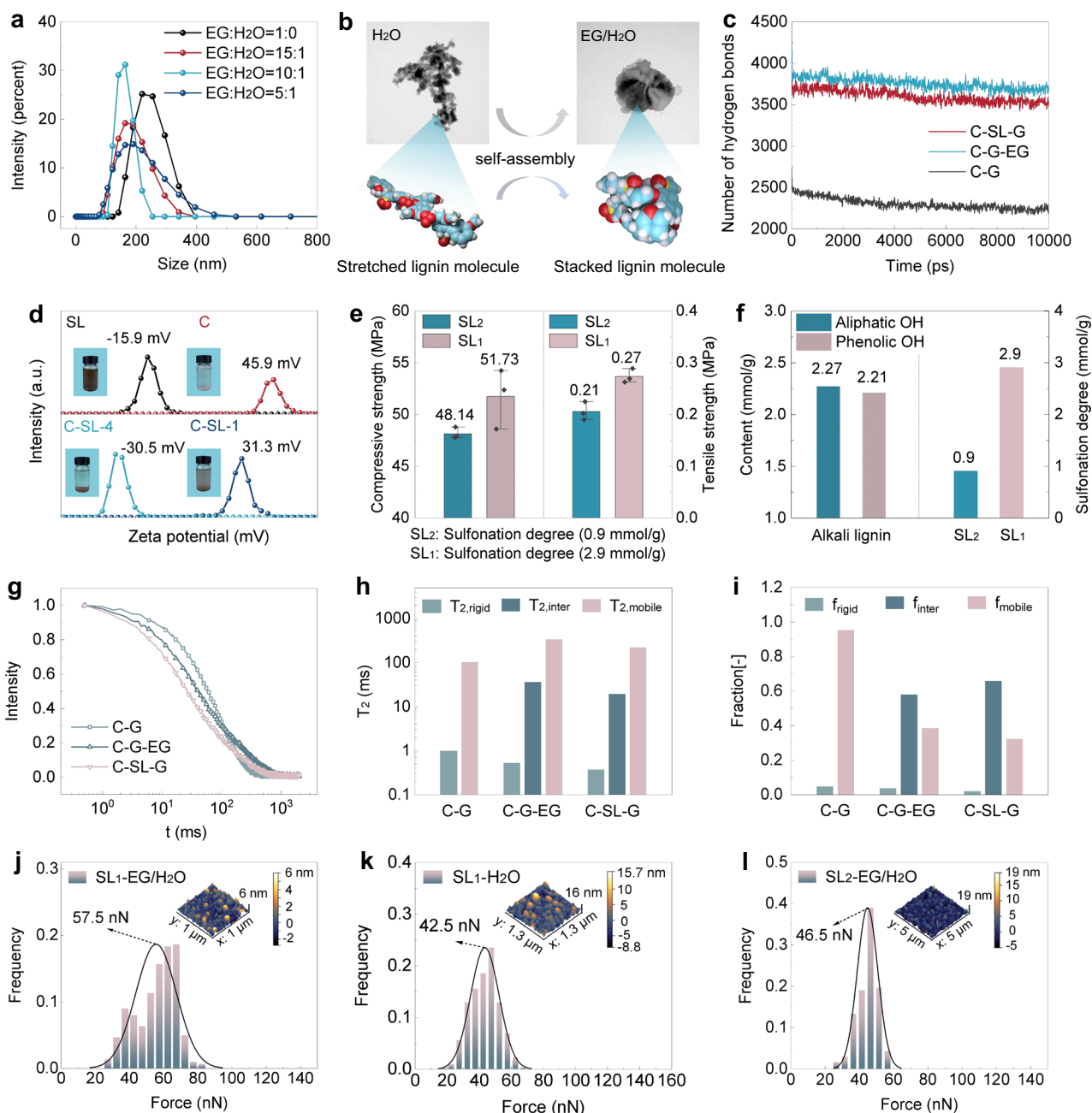
Fig. 4 | Enhanced mechanisms of the C-SL-G organohydrogels. a The particle size changes before and after the introduction of SL into the gel were simulated. **b** TEM images of lignin and conformations of lignin molecules in different solvents. Blue, red, yellow, and white represent C, O, S, and H elements, respectively. **c** The number of hydrogen bonds of C-G hydrogel, C-G-EG, and C-SL-G organohydrogels. **d** Zeta potential change of SL introduction into chitosan solution. **e** Primitive alkali lignin hydroxyl group content and two SL sulfonate group contents. Values in **e** represent their means ± SDs from $n = 3$ independent samples. **f** Compressive and tensile strengths of two SL-based organohydrogels. **g–i** Low-field NMR spectroscopy. Fully refocused ^{1}H NMR FID (**g**) of C-G hydrogel, C-G-EG and C-SL-G organohydrogels. Fitting results of the fully refocused ^{1}H NMR FID: T_2 (**h**) and f (**i**) of the three gels. **j–l** Intermolecular interaction forces between lignin and chitosan in H_2O and EG. The insets are scanned topographic maps of lignin particles under different solvents.

force frequency distribution[36,53,54]. The interaction between SL_1 (2.9 mmol/g) dissolved in EG and chitosan was stronger (57.5 nN) compared to that in the aqueous solution (42.5 nN), suggesting that the introduction of EG significantly improved the interfacial interactions between the polymer networks. In contrast, SL_2 with a lower sulfonation degree (0.9 mmol/g), which was also dissolved in EG, exhibited a weaker interaction with chitosan compared to SL_1 that with a high sulfonation degree (2.9 mmol/g). This further proves the essential role of sulfonate groups in improving mechanical properties. In summary, the addition of SL (-SO₃H) with abundant oxygen-

containing functional groups into the gel network forms a strong physical crosslinking network through noncovalent interactions. The insets in Fig. 4j-l are scanned topographic maps of lignin particles under different solvents, where lignin nanoparticles with small size can be observed. This observation is consistent with TEM results (Supplementary Fig. 35), indicating that the large lignin particles with hundred nanometers are composed of loosely aggregated small lignin nanoparticles. This underscores the effectiveness of solvent transformation in facilitating noncovalent interactions, offering a straightforward yet potent strategy for enhancing the design of gels.

Versatility of the C-SL-G conjoined-network organohydrogels

Biocompatibility is a critical requirement for the use of gels as biomedical materials. The presence of positively charged chitosan/gelatin and negatively charged SL promotes cellular colonization and multiplication[25,55]. To assess their cytocompatibility, the C-SL-G organohydrogel infusions were used to culture mouse chondrogenic progenitor cells (*ATDC5*) and mouse embryonic mesenchymal stem cells (*C3H/10T1/2*), and the presence of live cells was assessed by MTT detection kit assay and live-dead cell staining. The results show that after 24 h of incubation, the cell survival rate of C-SL$_{1-0.01}$-G organohydrogel remains consistently above 95%, providing favorable conditions for cell growth. When the incubation time is extended to 48 h, the cell survival rate is still maintained at a high level (≥ 90%) (Fig. 5a, b), and almost all *NIH3T3* cells extracts that cultured for 48 h on C-SL$_{1-0.01}$-G organohydrogel show green fluorescence (Fig. 5c). In addition, the C-SL-G organohydrogel exhibits a strong adsorption capacity for proteins and promotes the expression of cytokines (Supplementary Figs. 36 and 37). These results suggest that the biologically derived C-SL-G organohydrogels demonstrate excellent cytocompatibility in vitro, potentially enhancing cell proliferation. This may be due to the fact that the C-SL-G organohydrogels are composed of biomolecules (chitosan, gelatin, and SL).

For further validation, we implanted C-G-EG and C-SL-G organohydrogels into the backs of mice at temperature of 20–26 °C and relative humidity of 40–70% with light set to an automatic 12-hour light-dark cycle (Fig. 5d, e). After 2 weeks of implantation, both hydrogels maintained structurally stable, while significant degradation was observed after 4 weeks. Notably, compared with the C-G-EG organohydrogel, the C-SL-G organohydrogel exhibits a stronger ability to maintain its original structure. The results of section staining show that there is no inflammatory reaction, such as swelling and turbidity, around either organohydrogel, indicating good biocompatibility. The adhesion and burst pressure assessments further confirm the promising potential of these materials as medical substrates (Supplementary Figs. 38 and 39). In addition, the inhibition of *S. aureus* and *E. coli* by the organohydrogel demonstrates the excellent antimicrobial properties of the C-SL-G organohydrogel, which is likely owned to -OH and -SO$_3$H from SL (Supplementary Fig. 40)[56]. Therefore, when exposed to the oxidizing microenvironment, the C-SL-G organohydrogel can effectively eliminate the reactive oxygen species and exert its antioxidant ability. In addition, the C-SL-G organohydrogel has excellent thermal stability, freezing resistance, and solvent retention (Supplementary Figs. 41–46). Unlike C-G hydrogel, the G' of the C-SL-G organohydrogel stays almost constant throughout the entire temperature range (Supplementary Fig. 41). It also maintains good structural integrity without any damage after being exposed to air and saline at high temperature (Supplementary Figs. 42 and 43). The C-SL-G organohydrogel consistently maintains a stable mechanical property after being stored at different temperatures (−20 °C, −196 °C, 80 °C) for a period of time and tested at room temperature (Supplementary Figs. 44–46). This stability is attributed to the establishment of robust hydrogen bonds between EG and water molecules and with polymer molecules (chitosan, gelatin) present in the organohydrogel. Such hydrogen bonding interactions lead to a reduction of the freezing point and vapor pressure, along with an increase in the strength of connections within the polymer molecules and between the polymers and EG molecules. Consequently, the material is able to effectively preserve its physical crosslinking structure over the entire temperature spectrum[57,58]. The good biocompatibility, mechanical properties, and thermal stability make C-SL-G organohydrogel a promising candidate for biomedical load-bearing materials.

In addition to its excellent biocompatibility, the C-SL-G organohydrogel also exhibits excellent ionic conductivity, which results from the inherently positively charged chitosan in the raw material and the introduction of numerous −SO$_3$H during the solvent exchange. The ionic conductivity of the examined samples at various temperatures is illustrated in Fig. 5f. It's evident that as the temperature decreases, there is a natural decline in ionic conductivity. Nevertheless, the C-SL-G organohydrogel manages to sustain a notably high level of ionic conductivity, even at the frigid temperature of −40 °C. Of note, the C-SL-G organohydrogel performs even better at a relatively high temperature of up to 80 °C, highlighting its high-temperature stability in terms of ion conduction. Figure 5g demonstrates the combined advantages of high ionic conductivity, good mechanical properties, and frost resistance of the C-SL-G organohydrogel. The C-SL-G organohydrogel connectors exhibit varying degrees of changes in light-emitting diode (LED) brightness when twisted and pressed. Even at a low temperature of −20 °C, The C-SL-G organohydrogel can still emit light, which, combined with their excellent mechanical properties, makes C-SL-G organohydrogel a competitive material for ionic and biomedical applications.

To further validate the stable flexibility and conductivity of the organohydrogels, the rate of change of electronic resistance ($\Delta R/R_0 = (R_0-R)/R_0$; R_0 and R are corresponded to the resistance when unstretched and stretched, respectively) was used as a strain function, the relative resistance changes of the C-SL-G organohydrogel under different deformation modes were investigated. Wearable devices for monitoring body movements and other bio signals were fabricated using C-SL-G organohydrogel sensors. These sensors can monitor large-scale movements of the human body. Figure 5h provides comparative plots of the relative resistance change rate of the hydrogel sensors at finger bending angles of 30°, 45°, 60°, and 90°. The larger the finger bending angle, the higher the relative resistance. Figure 5i depicts the resistive response of the C-SL-G strain sensor to elbow flexion at different temperatures. It is observed that the C-SL-G strain sensor can detect and differentiate between extension and flexion motions of the joints.

The lack of significant differentiable signal attenuation at 25 °C and −20 °C suggests that the device can successfully maintain excellent strain sensitivity, thanks to the freezing resistance of the C-SL-G organohydrogel (Supplementary Fig. 47). We anticipate that our supramolecular organohydrogel with excellent anti-freezing properties can be potentially applied in low temperature adaptable batteries and sensors used in cold areas on earth and even in the realm of space exploration. Figure 5j shows that the signal strength of the strain sensor maintains stable even after one week of sealed storage, and has impressive resistance to electrical stability. This indicates that organohydrogels exhibit high strain sensitivity, making them a highly promising material for strain sensors.

Discussion

In this work, a "bottom-up" solution interface induced self-assembly strategy is adopted to develop a compressible, anti-fatigue, extreme environment adaptable, biocompatible, and recyclable chitosan-lignosulfonate-gelatin organohydrogel. The synergistic energy dissipation mechanism arising from noncovalent bonded conjoined network results in excellent mechanical properties and versatility for the organohydrogels. Furthermore, the solvent induced homogeneous nanoparticles of lignosulfonate enhance the crosslinking sites. Notably, the strength has exceeded that of conventional C-G hydrogels by more than 100 times. In addition to the high compressive strength, toughness, and fatigue resistance, the developed organohydrogel also demonstrates good biocompatibility both in vivo and vitro and environment adaptability at low temperature. Meanwhile, the organohydrogel presents low-cost processing and environmental sustainability through the utilization of all natural components and facile recyclability. Overall, this work displays a versatile approach to develop a resilient and tough organohydrogel based on electrostatic and hydrogen bonding interactions. We believe that the biologically sourced organohydrogels hold great potential for applications in areas
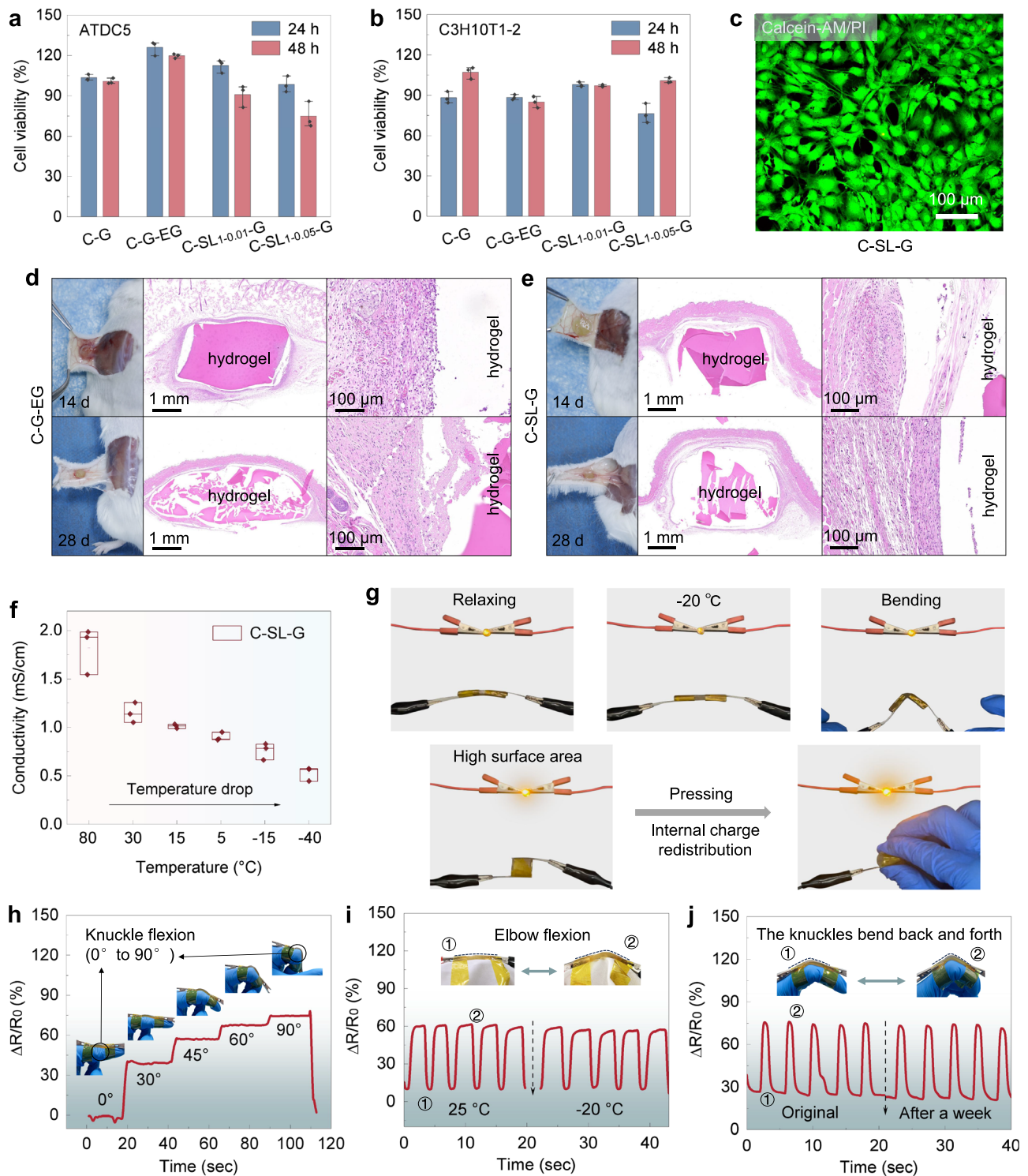
Fig. 5 | Versatility of the C-SL-G organohydrogels. Cell viability of *ATDC5* cells (**a**) and *C3H10T1-2* cells (**b**) cultured on the C-G hydrogel, C-G-EG, and C-SL-G organohydrogels for 24 and 48 h. Data in **a** and **b** represent their means ± SDs from $n = 3$ independent samples. **c** Confocal fluorescence microscopy images of *NIH3T3* cells cultured on C-SL$_{1-0.01}$-G organohydrogel immersion solution for 48 h. Scale bar, 100 μm. Grafting and staining images of C-G-EG (**d**) and C-SL$_{1-0.01}$-G organohydrogel (**e**) subcutaneously implanted in mice for 14 and 28 days after implantation. Inflammatory response to the implants was assessed by HE staining. **f** Ionic conductivity of C-SL$_{1-0.01}$-G organohydrogel at different temperatures. Center line = median; box limits = upper and lower quartiles; whiskers = 1.5× interquartile range ($n = 3$). **g** Photographs of C-SL$_{1-0.01}$-G organohydrogel connected into loops by bending, pressing, and at −20 °C. Relative resistance changes of C-SL$_{1-0.01}$-G organohydrogel under repetitive strain loading for fingers were flexed to different degrees (**h**) elbow joints were flexed back and forth at different temperatures (**i**) and fingers were flexed back and forth at a certain angle after being left for a week (**j**).

such as tissue engineering, vibration dampening, soft robotics, and smart wearable devices.

Methods

Ethics statement

All animal procedures were approved by the Animal Experimentation Ethics Committee of Research Selection Biotechnology (Hangzhou) Co., LTD (permission number SYXK (Zhejiang) 2021-0043). Informed consent has been obtained from all participants or their legally authorized representatives for this study.

Materials

Chitosan (deacetylation degree ≥95%, viscosity 100–200 mPa·s) was purchased from Shanghai Aladdin Biochemical Technology Co., Ltd. Gelatin (gum strength ~250 g Bloom) was purchased from Shanghai Maclean Biochemical Technology Co., Ltd. Kraft lignin (KL) was purchased from Jiangsu Paper Mill. Acetic acid (HAc, ≥99.8%), and formaldehyde (37 wt. % in H_2O), and poly (diallyl dimethylammonium chloride) solution (PDADMAC, 35 wt.% in H_2O) were purchased from Shanghai Aladdin Biochemical Technology Co., Ltd. EG (≥ 98%), and anhydrous sodium sulfite (Na_2SO_3, ≥98%), and glycerol (≥99%), and copper(II) sulfate anhydrous ($CuSO_4$, ≥98%), and sodium hydroxide (NaOH, >96%) were purchased from Shanghai Sinopharm Chemical Reagent Co., Ltd. *ATDC5* cells (CL-0856), and *C3H/10T1/2* cells (CL-0325), and *NIH3T3* cells (CL-0171) were purchased from Wuhan Pricella Biotechnology Co., Ltd. Live-dead staining reagent, and hematoxylin, and eosin staining reagents were purchased from Shanghai Bestbio Biotechnology, Co., Ltd. Mouse TGF-β1 ELISA Kit was purchased from Abcam, and the anti-TGF-β1 monoclonal antibody was diluted at a ratio of 1:100 in Assay Buffer. The strains of Escherichia coli (*E. coli*, ATCC 25922) and Staphylococcus aureus (*S. aureus*, CMCC (B) 26003) were obtained from Promega. All other chemicals were of analytical grade.

Preparation of lignosulfonates

KL was sulfonated to prepare lignosulfonates with different degrees of sulfonation. Briefly, 0.4 mL of 37% formaldehyde, 5.0 g of Na_2SO_3 and 10 g of KL were mixed with 30 mL of deionized water in a 100 mL stainless steel reactor. The reactor was heated to 140 °C in an oil bath and kept for 3 h to obtain SL_1. The content of sulfonate group in SL_1 was 2.9 mmol/g[59]. In addition, 10 g of KL was put into a high-pressure glass flask, 50 mL of NaOH solution (0.8 M) was added and dissolved under magnetic stirring, then 1.5 mL of formaldehyde was added, and after magnetic stirred at 70 °C for 1.5 h, 2 g of Na_2SO_3 was added and heated at 95 °C for 3 h to obtain SL_2. The content of sulfonate group in SL_2 was 0.9 mmol/g.

Preparation of C-SL-G organohydrogels

C-SL-G organohydrogels were prepared by simple gelation and solvent exchange. Briefly, the required amounts of chitosan (3%, w/v) and gelatin (15%, w/v) were dissolved in acetic acid aqueous solution (1%, v/v). The solution was stirred at 60 °C and then poured into the mold to form the original C-G composite hydrogel at 4 °C. The preformed hydrogels were further immersed in different concentrations of SL-EG solutions for 2-12 h (depending on sample size) to obtain C-SL-G organohydrogels.

Characterizations of different hydrogels and organohydrogels

TEM and SEM of lignin particles, C-G hydrogel, C-G-EG organohydrogel and C-SL-G (at 0.01 and 0.05 g/mL) organohydrogels were conducted using JEM-1400 (JEOL, Japan) and Quanta 200 (FEI, USA) instruments to observe the microstructure. Raman spectroscopy and spatial Raman mapping were performed utilizing confocal in situ Raman spectroscopy (LabRAM HR Evolution, Horiba, France), the wavelength of the excitation laser was 785 nm, and the image pixel size was 2.0 μm. FTIR of the samples were collected with FTIR spectrometer (VERTEX 80 V,

Bruker, Germany) in the frequency range of 4000–500 cm^{-1} with a total of 32 scans and a resolution of 4 cm^{-1}. The rheological characteristics of the gels were determined by a micro-infrared coupled rheometer (MARS60, Thermo Fisher, Germany), which measured the G′ and G″ of the gels at different shear forces and frequency, and recorded the G′ of the gels in the temperature range of 25–100 °C. Thermodynamic properties of the gels were tested by using DSC 214 Polyma (Netzsch, Germany) at a nitrogen flow rate of 40 mL/min. Statistical analysis of zeta potential and particle size distribution were performed by nano-laser particle size analyzer (Zetasizer Nano ZS, Malvern Panalytical, UK). The lignin sulfonation degree was tested using multifunctional automatic titrator (CT-1Plus, Hogon, China). XPS spectroscopy was obtained by Thermo Scientific K-Alpha (Thermo Fisher, USA), used to explore the chemical composition and the element binding energy changes of gels. Low-field NMR test was conducted using the VTMR20-010V-T NMR instrument (Niumag, China), T_2 measurements of the gels were conducted at a proton resonance frequency of 21 MHz (0.5 T). ^{31}P NMR spectroscopy and 2D-NMR spectroscopy were tested by 600 MHz fully digital superconducting NMR spectrometer (AVANCE III HD, Bruker BioSpin, Switzerland). Fatigue experiments were carried out using LTM 10 testing machine (ZwickRoell, Germany), high-frequency testing at 10 Hz and low-frequency testing at 1 Hz. Data were plotted using OriginPro 2022 SR1 (9.9.0.225) software.

Statistics and reproducibility

All experiments were repeated independently with similar results at least three times.

Reporting summary

Further information on research design is available in the Nature Portfolio Reporting Summary linked to this article.

Data availability

The data that support the findings of this study are available within this paper and/or included in the Supplementary Information, and from the corresponding authors upon request. Source data are provided with this paper.

References

1. Fu, L. L. et al. Cartilage-like protein hydrogels engineered via entanglement. *Nature* **618**, 740–747 (2023).
2. Feng, Y. H., Wang, Y. F., Chen, C. J., Wang, Z. H. & Liu, J. Bioinspired multiscale regulation for hydrogels with superior mechanics. *Innov. Mater.* **2**, 100105 (2024).
3. Han, Z. L. et al. A versatile hydrogel network–repairing strategy achieved by the covalent-like hydrogen bond interaction. *Sci. Adv.* **8**, eabl5066 (2022).
4. Sun, T. L. et al. Physical hydrogels composed of polyampholytes demonstrate high toughness and viscoelasticity. *Nat. Mater.* **12**, 932–937 (2013).
5. Yu, H. C. et al. Engineering tough metallosupramolecular hydrogel films with kirigami structures for compliant soft electronics. *Small* **17**, e2103836 (2021).
6. Zhang, Y. S. & Khademhosseini, A. Advances in engineering hydrogels. *Science* **356**, eaaf3627 (2017).
7. Sun, X. Y. et al. Green regenerative hydrogel wound dressing functionalized by natural drug-food homologous small molecule self-assembled nanospheres. *Adv. Funct. Mater.* **32**, 2106572 (2022).
8. Jiang, L. B. et al. Salt-assisted toughening of protein hydrogel with controlled degradation for bone regeneration. *Adv. Funct. Mater.* **29**, 1901314 (2019).
9. Guan, Q. F. et al. Bio-inspired lotus-fiber-like spiral hydrogel bacterial cellulose fibers. *Nano Lett.* **21**, 952–958 (2021).

10. Freedman, B. R. et al. Enhanced tendon healing by a tough hydrogel with an adhesive side and high drug-loading capacity. *Nat. Biomed. Eng.* **6**, 1167–1179 (2022).

11. Yu, S. X., Chen, L., Xie, Y. M., Feng, Q. H. & Chen, C. J. Lignin/polysaccharide composite: A nature-made match toward multifunctional bio-based materials. *Prog. Mater. Sci.* **148**, 101383 (2025).

12. Zhu, Q. L. et al. Light-steered locomotion of muscle-like hydrogel by self-coordinated shape change and friction modulation. *Nat. Commun.* **11**, 5166 (2020).

13. Liu, J. J., Qu, S. X., Suo, Z. G. & Yang, W. Functional hydrogel coatings. *Natl Sci. Rev.* **8**, nwaa254 (2021).

14. Zhang, M. C. et al. Hydrogel muscles powering reconfigurable micro-metastructures with wide-spectrum programmability. *Nat. Mater.* **22**, 1243–1252 (2023).

15. Li, X., Nakagawa, S., Tsuji, Y., Watanabe, N. & Shibayama, M. Polymer gel with a flexible and highly ordered three-dimensional network synthesized via bond percolation. *Sci. Adv.* **5**, eaax8647 (2019).

16. Ngai, T., Wu, C. & Chen, Y. Origins of the speckles and slow dynamics of polymer gels. *J. Phys. Chem. B* **108**, 5532–5540 (2004).

17. Zou, S. B., Therriault, D. & Gosselin, F. P. Spiderweb-inspired, transparent, impact-absorbing composite. *Cell Rep. Phys. Sci.* **1**, 100240 (2020).

18. Liu, C. et al. Tough hydrogels with rapid self-reinforcement. *Science* **372**, 1078–1081 (2021).

19. Sun, J. Y. et al. Highly stretchable and tough hydrogels. *Nature* **489**, 133–136 (2012).

20. Li, Y. X., Yan, J. H., Liu, Y. J. & Xie, X. M. Super tough and intelligent multibond network physical hydrogels facilitated by $Ti_3C_2T_x$ MXene nanosheets. *ACS Nano* **16**, 1567–1577 (2022).

21. Meng, X. H. et al. Hysteresis-free nanoparticle-reinforced hydrogels. *Adv. Mater.* **34**, 2108243 (2022).

22. Lei, W. W. et al. Diffusion–freezing-induced microphase separation for constructing large-area multiscale structures on hydrogel surfaces. *Adv. Mater.* **31**, 1808217 (2019).

23. Wu, J. Y. et al. Strong and ultra-tough supramolecular hydrogel enabled by strain-induced microphase separation. *Adv. Funct. Mater.* **33**, 2210395 (2023).

24. Hua, M. T. et al. Strong tough hydrogels via the synergy of freeze-casting and salting out. *Nature* **590**, 594–599 (2021).

25. Xu, L. J. et al. Conjoined-network rendered stiff and tough hydrogels from biogenic molecules. *Sci. Adv.* **5**, eaau3442 (2019).

26. Xu, L. J. et al. A solvent-exchange strategy to regulate noncovalent interactions for strong and antiswelling hydrogels. *Adv. Mater.* **32**, 2004579 (2020).

27. Dong, X. Y. et al. Strong and tough conductive organo-hydrogels via freeze-casting assisted solution substitution. *Adv. Funct. Mater.* **32**, 2203610 (2022).

28. Xu, X. W., Jerca, V. V. & Hoogenboom, R. Bioinspired double network hydrogels: from covalent double network hydrogels via hybrid double network hydrogels to physical double network hydrogels. *Mater. Horiz.* **8**, 1173–1188 (2021).

29. Kamata, H., Akagi, Y., Kayasuga-Kariya, Y., Chung, U. & Sakai, T. Nonswellable" hydrogel without mechanical hysteresis. *Science* **343**, 873–875 (2014).

30. Wang, S. H. et al. Strong, tough, ionic conductive, and freezing-tolerant all-natural hydrogel enabled by cellulose-bentonite coordination interactions. *Nat. Commun.* **13**, 3408 (2022).

31. Liu, Y. N. et al. Construction of chitosan-based hydrogel incorporated with antimonene nanosheets for rapid capture and elimination of bacteria. *Adv. Funct. Mater.* **30**, 2003196 (2020).

32. Zhang, Q. et al. Extremely strong and tough chitosan films mediated by unique hydrated chitosan crystal structures. *Mater. Today* **51**, 27–38 (2021).

33. Scatena, L. F., Brown, M. G. & Richmond, G. L. Water at hydrophobic surfaces: weak hydrogen bonding and strong orientation effects. *Science* **292**, 908–912 (2001).

34. Li, M. et al. Comprehensive H_2O molecules regulation via deep eutectic solvents for ultra-stable zinc metal anode. *Angew. Chem. Int. Ed.* **62**, e202215552 (2023).

35. Feng, Y. F. et al. Solvent-induced in-situ self-assembly lignin nanoparticles to reinforce conductive nanocomposite organogels as anti-freezing and anti-dehydration flexible strain sensors. *J. Chem. Eng.* **433**, 133202 (2022).

36. Zhang, X., Liu, W. F., Yang, D. J. & Qiu, X. Q. Biomimetic supertough and strong biodegradable polymeric materials with improved thermal properties and excellent UV-blocking performance. *Adv. Funct. Mater.* **29**, 1806912 (2019).

37. Wang, Y., Li, F. B., Fang, W. H., Sun, C. L. & Men, Z. W. Study of hydrogen bonding interactions in ethylene glycol-water binary solutions by Raman spectroscopy. *Spectrochim. Acta A Mol. Biomol. Spectrosc.* **260**, 119916 (2021).

38. Wu, Q. et al. Steady and dynamic rheological behaviors of sodium carboxymethyl cellulose entangled semi-dilute solution with opposite charged surfactant dodecyl-trimethylammonium bromide. *J. Colloid Interface Sci.* **339**, 236–242 (2009).

39. Jiang, P. et al. 3D Printing of dual-physical cross-linking hydrogel with ultrahigh strength and toughness. *Chem. Mater.* **32**, 9983–9995 (2020).

40. Afewerki, S. et al. Combined catalysis for engineering bioinspired, lignin-based, long-lasting, adhesive, self-mending, antimicrobial hydrogels. *ACS Nano* **14**, 17004–17017 (2020).

41. Zhang, L. et al. Cellulose nanofiber-mediated manifold dynamic synergy enabling adhesive and photo-detachable hydrogel for self-powered E-skin. *Nat. Commun.* **15**, 3859 (2024).

42. Zhao, Z. G., Fang, R. C., Rong, Q. F. & Liu, M. J. Bioinspired nanocomposite hydrogels with highly ordered structures. *Adv. Mater.* **29**, 1703045 (2017).

43. Kim, J., Zhang, G. G., Shi, M. X. Z. & Suo, Z. G. Fracture, fatigue, and friction of polymers in which entanglements greatly outnumber cross-links. *Science* **374**, 212–216 (2021).

44. Sun, W. X. et al. Molecular engineering of metal coordination interactions for strong, tough, and fast-recovery hydrogels. *Sci. Adv.* **6**, eaaz9531 (2020).

45. Chen, L. H. et al. New insight into lignin aggregation guiding efficient synthesis and functionalization of a lignin nanosphere with excellent performance. *Green. Chem.* **24**, 285–294 (2022).

46. Wang, J. F., Zhang, D. H. & Chu, F. X. Wood-derived functional polymeric materials. *Adv. Mater.* **33**, 2001135 (2021).

47. Chen, F. et al. Rational fabrication of anti-freezing, non-drying tough organohydrogels by one-pot solvent displacement. *Angew. Chem. Int. Ed.* **57**, 6568–6571 (2018).

48. Gao, Y. et al. Critical effect of segmental dynamics in polybutadiene/clay nanocomposites characterized by solid state 1H NMR spectroscopy. *J. Phys. Chem. C.* **118**, 5606–5614 (2014).

49. Chen, S. J., Wu, G. P., Wang, X. L., Chen, X. X. & Nealey, P. Sub–10 nm feature sizes of disordered polystyrene-block-poly(methyl methacrylate) copolymer films achieved by ionic liquid additives with selectively distributed charge interactions. *ACS Appl. Polym. Mater.* **2**, 427–436 (2020).

50. Liu, L. L. et al. A Superstrong and reversible ionic crystal-based adhesive inspired by ice adhesion. *Angew. Chem. Int. Ed.* **60**, 8948–8959 (2021).

51. Di, X., Hou, J. W., Yang, M. M., Wu, G. L. & Sun, P. C. A bio-inspired, ultra-tough, high-sensitivity, and anti-swelling conductive hydrogel strain sensor for motion detection and information transmission. *Mater. Horiz.* **9**, 3057–3069 (2022).

52. Hu, Y. et al. A "Two-in-One" strategy for flexible aqueous batteries operated at −80 °C. *Adv. Funct. Mater.* **32**, 2203081 (2022).

53. Allison, D. P., Hinterdorfer, P. & Han, W. H. Biomolecular force measurements and the atomic force microscope. *Curr. Opin. Biotech.* **13**, 47–51 (2002).

54. Fisher, T. E., Oberhauser, A. F., Carrion-Vazquez, M., Marszalek, P. E. & Fernandez, J. M. The study of protein mechanics with the atomic force microscope. *Trends Biochem. Sci.* **24**, 379–384 (1999).

55. Sharmeen, S. et al. Polyethylene glycol functionalized carbon nanotubes/gelatin-chitosan nanocomposite: An approach for significant drug release. *Bioact. Mater.* **3**, 236–244 (2018).

56. Das, A. K. et al. Lignin - A green material for antibacterial application — A review. *Int. J. Biol. Macromol.* **261**, 129753 (2024).

57. Ding, Q. L. et al. Environment tolerant, adaptable and stretchable organohydrogels: preparation, optimization, and applications. *Mater. Horiz.* **9**, 1356–1386 (2022).

58. He, Z. R. & Yuan, W. Z. Adhesive, stretchable, and transparent organohydrogels for antifreezing, antidrying, and sensitive ionic skins. *ACS Appl. Mater.* **13**, 1474–1485 (2021).

59. Gao, W. J., Inwood, J. P. W. & Fatehi, P. Sulfonation of hydroxymethylated lignin and its application. *J. Bioresour. Bioprod.* **4**, 80–88 (2019).

Author contributions

C.C., B.J., and Y.J. conceived the concept, processing, structure details and supervised the work. Y.G. and C.X. carried out most experiments and co-wrote the manuscript. C.C., B.J., Y.J., Y.G. and C.X. revised the manuscript. Y.W., J.L. and D.S. assisted in completing the photographs of samples in the manuscript. W.W. and L.C. contributed to the sample preparation and manuscript editing. All authors commented on the submitted version of the manuscript.

Competing interests

The authors declare no competing interests.

Additional information

Supplementary information The online version contains supplementary material available at https://doi.org/10.1038/s41467-024-55530-1.

Correspondence and requests for materials should be addressed to Yongcan Jin, Bo Jiang or Chaoji Chen.

Peer review information *Nature Communications* thanks Kai Tao and the other, anonymous, reviewers for their contribution to the peer review of this work. A peer review file is available.

Reprints and permissions information is available at http://www.nature.com/reprints

Publisher's note Springer Nature remains neutral with regard to jurisdictional claims in published maps and institutional affiliations.